



Propulsion Configuration Design and Analysis for an eVTOL Passenger Air Shuttle

Nina Ayar*, Mujahid Ahmed†, Kamil Nocon‡, Roshan Patel†, Timothy Green§, John D. Reband¶, and Kiruba S. Haran||
University of Illinois at Urbana-Champaign, Urbana, IL 61801

Abstract - This paper describes the design maturation of an electric vertical take-off and landing (eVTOL) aircraft for urban air mobility. This work aims to build upon previous work on the propulsion design to ensure the vehicle is stable and airworthy using GeneAI, a python based genetic algorithm. The design aspects used in the genetic algorithm for this study are wing position, planform dimensions, number of propulsors and their span-wise position. Additionally, a detailed powertrain configuration analyzed using Simulink is also presented. Aerodynamic efficiency of various propulsion configurations and power requirements will be evaluated and the final design presented.

I. Introduction

This paper describes the maturation of the aerodynamic and electrical systems design of the Illini Air Shuttle (IAS) in terms of vehicle configuration and powertrain design. It expands upon previous work that attempted to maximize the payload by trading wing aspect ratio, number of propulsors, and propulsive span [1]. While this study suggested an optimal number of propulsors and span for the distribution of propulsors by analyzing the effective power and wing loading, wing design and stability analysis has yet to be conducted. Thus, wing design and flight characteristics analysis are the obvious next steps to mature the design. The aerodynamic analysis is especially important due to the unconventional configuration. While the tandem wing design is desirable for distributing the propulsors for vertical flight, the interaction between the front and back wing should be analyzed to ensure the airworthiness of the design. The wing interaction effects also compound with the propeller-wing interaction (modeling of which is still an active research area).

In addition to aerodynamic analysis, the design of the powertrain is a necessary step to complete the conceptual vehicle design. The total mass, volume, and heat rejected from the powertrain components are important components to understand for system integration. Relevant tasks include topology selection and sizing of the machines, selection and sizing of the energy storage technology, control system design, and dynamic simulation to quantify the efficiency and stability of the power system. The goal is to determine the high-level specifications of the power system at a level of depth and confidence appropriate for conceptual aircraft design.

The motivation of developing the IAS concept is primarily to add to the publicly available body of design work on electric aircraft. While there has been no shortage of vehicle concepts generated in recent years by both startup and established airframers, detailed specifications of matured designs are typically not made freely available. One notable exception is a set of reference vehicles developed by NASA [2]. The availability of such information supports the development of relevant component technologies and ancillary systems by allowing researchers to understand the qualities of electric aircraft designs that are most likely to enter service. Additionally, meta-research on published designs may help identify and track required improvements in contemporary technology needed to realize practical electric flight; this would be especially useful for energy storage and power electronic equipment. In short, publicly available design data on a large set of electric aircraft is valuable for researchers working on related technology and can provide perspective on the state of design techniques.

*Undergraduate Researcher, Industrial and Enterprise Systems Engineering, UIUC

†Undergraduate Researcher, Aerospace Engineering, UIUC

‡Undergraduate Researcher, Mechanical Science and Engineering, UIUC

§Undergraduate Researcher, Electrical and Computer Engineering, UIUC

¶Graduate Research Assistant, Electrical & Computer Engineering, UIUC

|| Professor, Electrical & Computer Engineering, UIUC, Associate Fellow AIAA

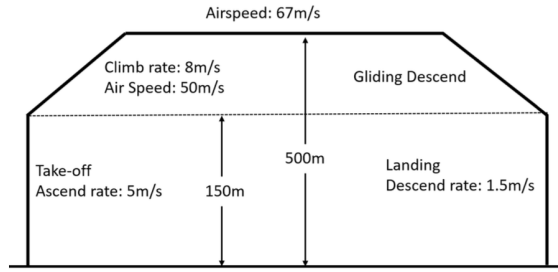


Figure 1 Mission Profile

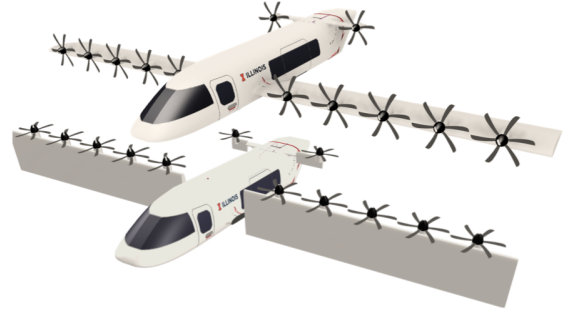


Figure 2 Notional IAS design in cruise (top) and takeoff/landing (bottom) configuration

II. Background

A concept for a vectored thrust eVTOL aircraft has been developed for transportation between cities separated by a distance between 200km and 300km, and was presented in Xiao et. al [1]. The aircraft will address limitations of existing methods of public transportation such as unreliable railroad systems and slow buses/shuttles. The aircraft will carry ten people and follow the mission profile shown in Figure 1.

Due to its high speed and ability to take-off and land in a metropolitan area, an eVTOL aircraft is a desired alternative to current methods of transportation. Traveling by eVTOL also drastically reduces emissions and transit time. The vectored thrust technology has been selected for its high efficiency and endurance compared to other eVTOL aircraft technologies.

Existing designs of manned eVTOL aircraft fall into the following categories: the multi-rotor configuration, the lift-and-cruise configuration, and the tilt-rotor configuration. This design utilizes the tilt-rotor configuration in which the wings and propellers tilt to allow for optimal performance during take-off, cruise and landing.

The proposed eVTOL aircraft shown in Figure 2 details a 12-propeller tilted rotor-wing design with a distributed propulsion system. This concept has been optimized iteratively to provide a high-level representation of the trade-offs between range and payload. Vehicle parameters such as wing aspect ratio, number of propulsors, and propulsive span were varied using a genetic algorithm based optimization tool, GOSET in attempts to maximize the payload. Increasing electric motor specific power was also studied to determine its effects on aircraft performance. However, results indicated that increasing the specific power did not largely affect payload capacity. The resulting aircraft's specifications are given in Table 1.

Item	Value
Transit Time [min]	64
Total Mass [kg]	3575
Aspect Ratio	13.7
Wing Area [m^2]	26.12
Number of Propellers	12
Radius of Propeller [m]	0.75
Payload [kg]	1000
Wing Loading [kg/m^2]	126.9
Total Energy [kWh]	537
Motor Specific Power [kW/kg]	10
Motor Mass [kg]	95.4
Power Overload Factor	1.28

Table 1 Proposed Design Specifications

The first phase of flight indicated in the vehicle's mission profile is vertical take-off from a parking lot or other open area and climb to a minimum building clearance of 150 meters at a rate of 5m/s. In the second phase, the wings and propellers tilt forward to transition the aircraft into a horizontal climb and an airspeed of 50m/s. Once the aircraft reaches an altitude of 500m, the vehicle initiates the third phase and levels off to cruise at 67m/s towards its final destination. Upon nearing the destination, the fourth phase is initiated and the aircraft glides to an altitude of 150m. In the fifth and final phase, the wings and propellers of the air shuttle tilt upwards consistent with a vertical landing configuration and descends at a rate of 1.5m/s. The expected mission profile parameters of each phase are listed in Table 2 with the thrust requirements displayed graphically in Figure 3. Please note that the cruise section of the mission profile is much longer than the other portions and was scaled down in Figure 3 for presentation purposes.

Phase	Duration (s)	Thrust Required (N)
1	30	35034
2	44	6428
3	2875	1752
4	105	0
5	100	35034

Table 2 Mission Profile Parameters

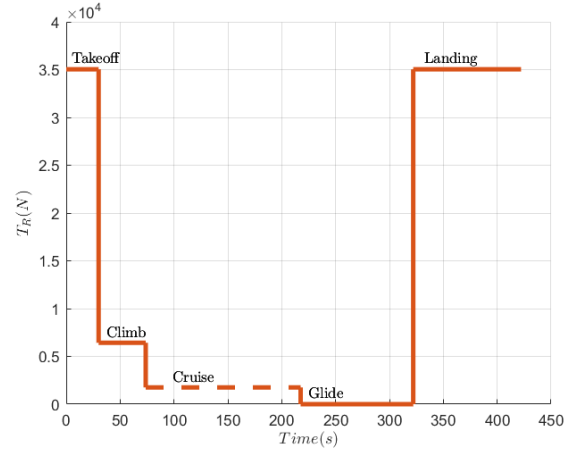


Figure 3 Vehicle thrust over time for each phase of the mission

III. Vehicle Configuration

In order to mature the design presented in Xiao et. al [1], a single-target optimization technique was performed to determine an optimal distribution of wing area and wing position that provides acceptable flight performance within acceptable stress. The software package of choice to evaluate aerodynamic performance was the VSPAERO inviscid solver (packaged with OpenVSP) and the GeneAl genetic algorithm python library. The methodology is illustrated graphically in Figure 4.

A. Initial Design

Following the high-level vehicle design specified in [1], the design configuration was refined to ensure a geometry for balanced, steady horizontal flight at altitude. The updated design specifications are shown in Table 3. This refined configuration served as a population initializer for the genetic algorithm. Total wing area ($47.432m^2$), aspect ratio (12.1), and number of propellers (12) [1] were kept constant across all individuals to preserve the overall cruise weight and lifting capabilities.

Propeller coefficients calculated for the purpose of this study were loosely based off the XV-15 prop-rotors. While the scale of the blades is significantly larger than those for the purposes of the Air Shuttle, it is expected that the similar design intent for vertical and horizontal flight equates to a reasonable representation of the propellers to be used with the Air Shuttle. The thrust and power coefficients are stated below [3]:

$$C_t = 0.012$$

$$C_p = 0.0012$$

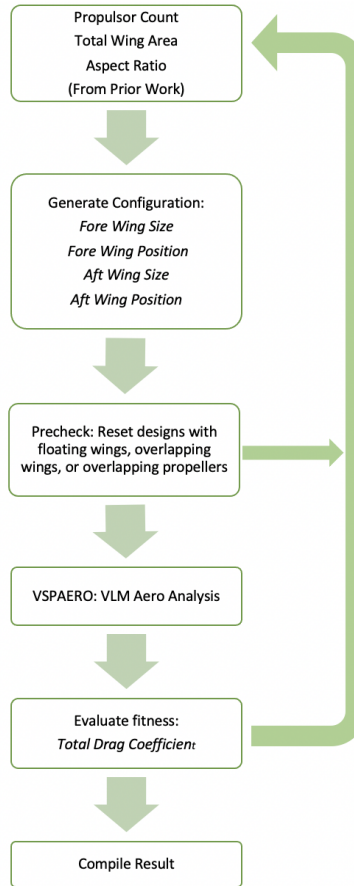


Figure 4 Genetic optimization process flowchart

Item	Value
Wing Span	16.94 m
Wing Chord	1.4 m
Wing Area (Per Wing)	23.716 m^2
Aspect Ratio	12.1
Wing Airfoil	NACA 2415
Fore Wing Tip Location	X = 3.261, Z = 0.1
Aft Wing Tip Location	X = 8.5, Z = 1.87
Fuselage Length	11.868 m
Fuselage Width	3 m
Fuselage Height	2 m
Number of Propellers	12

Table 3 Updated Design Specifications

B. Genetic Algorithm Parameters

To validate the optimization, a population size of 50 individuals (or chromosomes) was generated over 100 generations with a mutation rate of 0.15. The resulting sample size of 5,000 randomly generated and mutated configurations was deemed an appropriate sample size to study the correlation between design configurations and aerodynamic performance.

All individuals were defined by the dimensions and positions of each wing, with the combined total wing area and aspect ratio kept constant from previous work [1]. Each individual had a unique combination of five genes (or variables): the x-positioning of the fore wing (X1), the z-positioning of the fore wing (Z1), the x-positioning of the aft wing (X2), the z-positioning of the aft wing (Z2), and the wing area split between the fore and aft wings (AS). Each individual's combination of genes can also be referred to as its chromosome. The x-position aligns with the length of the fuselage, while the z-position aligns with the height of the fuselage. Each gene had a specified range from which the algorithm could randomly select values for each design. The ranges were set in place to ensure no designs which defied logic were analyzed. The wing area split is expressed as a ratio of the area of the front wing to the total allotted wing area ($47.432m^2$). The minimum and maximum values specified for each gene are given in Table 4.

Variable	Minimum	Maximum
X1 (m)	2.5	7
Z1 (m)	0	2
X2 (m)	2.5	11
Z2 (m)	0	2
AS	0.1	0.85

Table 4 Design Space Boundaries

To ensure feasible geometries when implementing the genetic algorithm, checks were added to ensure configurations with characteristics that defied logic such as floating wings, overlapping wings and/or propellers would not arise.

To prevent overlapping between the fore wing and aft wing, it was required that there be at least a chord length of space between the x-position of both wings. If this condition was not satisfied, the x-position of the aft wing was adjusted by the difference between the maximum chord length and the distance between the wings in the configuration.

The number of propellers for the aft wing and fore wing were calculated respectively using equations 1 and 2.

$$P_a = 2 \times \left\lceil \frac{\left[\frac{12}{\frac{s_f}{s_a} + 1} \right]}{2} \right\rceil \quad (1)$$

$$P_f = 12 - P_a \quad (2)$$

where

s_f = wingspan of fore wing

s_a = wingspan of aft wing

The spacing between each propeller was calculated as the ratio between the wingspan and the number of propellers on a given wing. As specified in Table 1, previous work necessitated a propeller radius of 0.75m. To prevent interference between propellers, the minimum distance between the center of each propeller was set to 1.5m. Individuals with propellers that failed to satisfy this condition were manually set to have a distance of 1.5m between propellers.

The target of the genetic algorithm was to minimize the total drag coefficient at cruise conditions (Angle of attack = 2°) to provide a baseline cruise performance. While the aerodynamics and stability of the transition from vertical to horizontal flight poses the biggest design challenge, optimizing the vehicle configuration at cruise via the genetic algorithm requires significantly less computation time per individual and provides a control to be iterated upon in future work.

C. Parameter Selection

The individual wing positioning and sizing were selected as genes in the genetic algorithm to account for the aerodynamic interactions each wing imposes on the other. Previous trade studies of biplane aerodynamics show that the flow field is negatively altered in the form of a weaker pressure distribution when the wings are too close to each other in the x and z directions. A drastic change in the pressure distribution such as this would lead to implications including a reduction in produced lift, especially at low speeds. However, this effect can be minimized by manipulating

the separation of the wings in both x and z directions to provide the maximum amount of distance between the two wings [4]. Furthermore, the propulsion configuration of the Air Shuttle effectively creates a blown wing arrangement and further modifies the flow field. Not only does each propulsor interact with adjacent propulsors and the wing to which it is mounted, but different performance is observed between the upstream and downstream set of propellers. Primarily, it has been shown that the vorticity in the propeller wake will reduce the available thrust of any downstream propellers caught in the wake [5].

Additionally, there are concerns regarding the effects of downwash, an effect cause by a spanwise movement of air along a wing, and wake vortices generated by the fore wing on the aft wing. While some tandem wing arrangements display favorable behavior in avoiding stall, the performance of the rear wing through the entire flight regime should be well understood to ensure the stability and overall airworthiness of the design [6] [7]. Given the x and z positions, wing area split, total wing area, and aspect ratio of both wings, the full plane and wing configuration, including chord and span of each wing, can be calculated and modeled in OpenVSP.

The coefficient of drag was chosen as the optimization target due to the direct relation between power required from the motors and drag. The relation demonstrated in equation 3 shows that less drag equates to less power required. By minimizing the required power, in theory, the motors and batteries can be sized down accordingly in terms of their technical capabilities.

$$P = DV \quad (3)$$

where

P = Power Required

D = Drag

V = Velocity

D. Simulation Results

All configurations produced by the genetic algorithm were put through a powered wing analysis using the Vortex Lattice Method in VSPAERO. The following VSPAERO settings— Mach Number, Angle of Attack, Thrust and Power Coefficients, Rotor Speed— were kept consistent across all individuals. The values shown below are representative of cruise conditions. For the purposes of this study, propellers were modeled as actuator disks in OpenVSP. Power requirements over the mission profile are discussed further in later sections.

Mach Number	0.2
Angle of Attack (alpha)	2.0
Coefficient of Thrust (C_T)	0.012
Coefficient of Power (C_P)	0.0012
Rotor Speed (rpm)	1291

Table 5 VSPAERO Settings

By default, the few individuals that resulted in a negative drag coefficient were immediately discarded and did not contribute to future generations. A potential cause for the negative coefficients can be attributed to the way VSPAERO calculates loads on aircraft due to spinning rotors. In the case of net thrust, it may appear as negative drag.

The chromosome of the best individual is as follows (5.70586062,0.63924198, 10.40016487, 0.80395107, 0.45037249) with values corresponding to X1, Z1, X2, Z2, and AS respectively. The best vehicle configuration is detailed in Table 6 and illustrated using the OpenVSP interface in Figure 5.

The minimum total drag coefficient achieved by the genetic algorithm was 0.0002 compared to 0.06296 of the starting individual. The curve in Figure 6 shows the general trend for total drag coefficient over generations. As expected, total drag decreases over each generation. The minimum drag coefficient decreases dramatically with the introduction of new individuals with superior drag coefficients. Over time the rate at which the minimum drag coefficient decreased diminished until it stabilized to an optimal result.

The drag coefficient was plotted against the difference in x-position between the wings, the difference in z-position between the wings, and the area split between the wings as seen in Figure 7. Outliers were removed to provide better

Item	Value
Fore Wing Span	16.08 m
Fore Wing Chord	1.39 m
Fore Wing Area	21.36 m^2
Aft Wing Span	17.76 m
Aft Wing Chord	1.47 m
Aft Wing Area	26.07 m^2
Aspect Ratio	12.1
Wing Airfoil	NACA 2415
Fore Wing Tip Location	X = 5.706, Z = 0.639
Aft Wing Tip Location	X = 10.400, Z = 0.804
Fuselage Length	11.868 m
Fuselage Width	3 m
Fuselage Height	2 m
Number of Propellers	12

Table 6 Best Vehicle Configuration

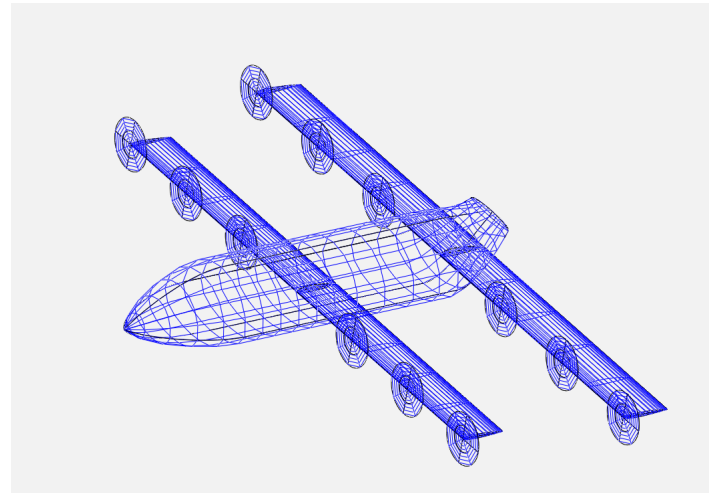


Figure 5 Graphical Depiction of Best Individual in OpenVSP

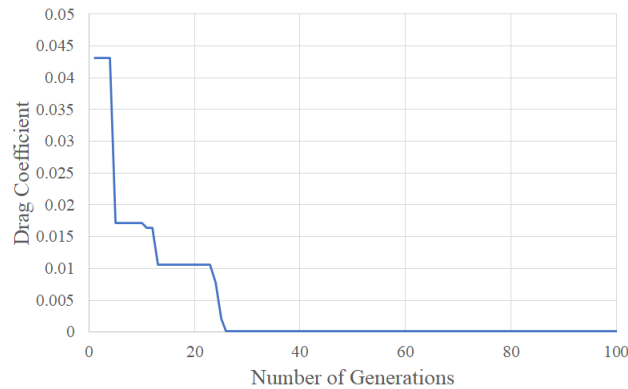


Figure 6 Minimum Drag Coefficient vs. Number of Generations

resolution of the data for presentation purposes. After plotting total drag against each gene's values, it does not appear that any variable singlehandedly has any discernible effect on minimizing drag, suggesting that the drag coefficient cannot be predicted by any one variable due to the many complex aerodynamic effects taking place.

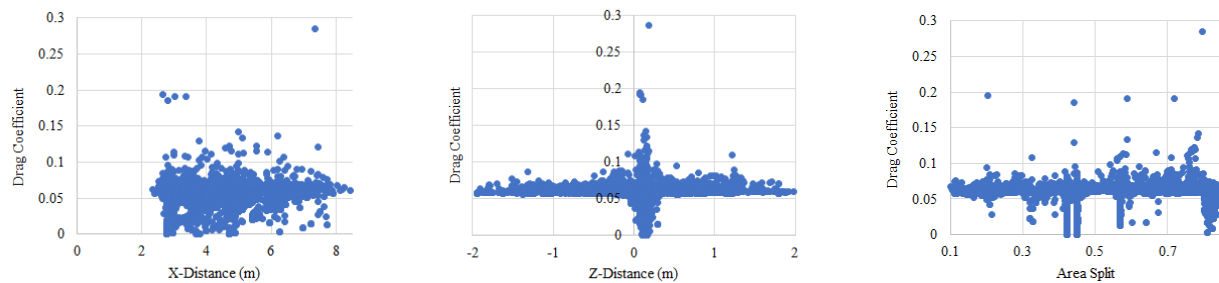


Figure 7 Wing Dimensions against Drag Coefficient

IV. Powertrain Design

Further analysis of a potential powertrain was performed through the selection and modeling of specific components using Simulink. The modeling was a continuation of the work and estimations done in [1] and provided a preliminary estimate of the weight, size, and available power of the electrical propulsive system. This model included the motor, inverter, battery, and control system.

A. Motor Modeling

A key consideration for electric propulsion is the weight of the components needed to provide power for the flight. Permanent Magnet Synchronous Machines (PMSM) can provide higher power densities and specific powers making them the ideal choice for this application [8]. Permanent Magnet Synchronous Machines can be further divided by the direction of flux. Radial flux machines produce magnetic flux along the radius of the machine while axial flux machines produce magnetic flux in the direction of the axis of rotation. Axial flux machines show larger torque and power densities than radial flux machines for high power applications [9]. The main drawback of axial flux machines with high power and torque is the large diameter. A larger rotor diameter leads to a larger edge speed and more stress on the rotor for a set rotational speed. Because of this, the maximum speed of these machines decreases as the rotor diameter and maximum torque output increases.

Our flight plan requires the most power and torque during the vertical takeoff and landing portions of the flight. Using the estimated weight of the aircraft and a standard helicopter propulsive power of 4 lbs/hp, it was determined that 1.47MW of power is needed at takeoff or landing. The aircraft was planned with 12 total propellers leading to about 123kW of power for each motor. Using the thrust (C_T) and power (C_P) coefficients mentioned previously, the required torque and speed of the motor for takeoff and landing was determined to be 238Nm and 4929rpm. With a high torque and low speed requirement as shown, the axial flux machine fit the application best and provided the highest specific power and power density available. The specific motor chosen for this vehicle was the EMRAX 268 Medium Voltage Axial Flux Motor. This motor has an advertised peak output power of 200kW and a rated speed of 4500rpm. The specifics of the motor parameters can be found in [10] and seen below in Table 7.

Peak Power	200 kW
Continuous Power	86 kW
Maximum Stator Current	400 A_{rms}
Continuous Stator Current	190 A_{rms}
Rated Maximum Rotor Speed	4500 rpm
Maximal Battery Voltage	650 V_{dc}
Per Phase Stator Resistance, R_s	10.5 m Ω
Per Phase Inductance, L_d/L_q	126/118 μH
Magnetic Flux, λ_f	0.0664 Wb
Number of Pole Pairs, p	10
Rotor Inertia, J	0.0922 kg * m ²
Weight	20 kg
Size	5.13 l

Table 7 EMRAX 268 Medium Voltage Axial Flux Motor Parameters

Every AC machine is powered by sinusoidal voltages and currents which make for complicated modeling and computationally heavy simulations. One common method used to simplify this modeling and the control method is the transformation to a rotating set of axes. The $d - q$ reference frame is a set of axes that rotate with the electrical frequency of the stator current and voltage. The transformation from a three phase sinusoidal value to the two phase rotating $d - q$ reference frame is called the Park Transform and results in a constant value for the two phases. The mathematical transformation between the three phase, or $a - b - c$ reference, to the $d - q$ reference and the inverse transform from the $d - q$ reference to the $a - b - c$ reference are shown below in equations 4 and 5 respectively [11]. The $d - q$ reference often has a third phase value known as the zero axis. This axis includes the effects of any unbalanced $a - b - c$ reference. This machine was assumed to be balanced for the purposes of this paper. Consideration of the zero

axis will be important for more in-depth analysis of the powertrain.

$$\begin{pmatrix} i_d \\ i_q \end{pmatrix} = \frac{2}{3} \begin{pmatrix} \cos(\theta) & \cos(\theta - \frac{2\pi}{3}) & \cos(\theta + \frac{2\pi}{3}) \\ -\sin(\theta) & -\sin(\theta - \frac{2\pi}{3}) & -\sin(\theta + \frac{2\pi}{3}) \end{pmatrix} \begin{pmatrix} i_a(\theta) \\ i_b(\theta) \\ i_c(\theta) \end{pmatrix} \quad (4)$$

$$\begin{pmatrix} v_a(\theta) \\ v_b(\theta) \\ v_c(\theta) \end{pmatrix} = \begin{pmatrix} \cos(\theta) & -\sin(\theta) \\ \cos(\theta - \frac{2\pi}{3}) & -\sin(\theta - \frac{2\pi}{3}) \\ \cos(\theta + \frac{2\pi}{3}) & -\sin(\theta + \frac{2\pi}{3}) \end{pmatrix} \begin{pmatrix} v_d \\ v_q \end{pmatrix} \quad (5)$$

where

$$\begin{aligned} v_a, v_b, v_c &= a - b - c \text{ reference stator voltage} \\ v_d, v_q &= d - q \text{ reference stator voltage} \\ i_a, i_b, i_c &= a - b - c \text{ reference stator current} \\ i_d, i_q &= d - q \text{ reference stator current} \\ \theta &= \text{electrical rotational position} \end{aligned}$$

Using this rotating reference frame, a mathematical model of the electrical aspects of the PMSM was created using equations 6 and 7 [12]. These equations relate the stator $d - q$ voltage to the magnetic flux linkages of the machine. The flux linkages are then related to the stator currents through equations 8 and 9. Our system controlled the PMSM through the stator voltage and received feedback through the mechanical speed and the stator currents. Solving for the stator currents using these previously mentioned equations results in equations 10 and 11 [12]. Note that the permanent magnet flux linkage, λ_f , does not change with time. Therefore, $\frac{d\lambda_f}{dt} = 0$.

$$v_d = R_s i_d + \frac{d\lambda_d}{dt} - \omega_e \lambda_q \quad (6)$$

$$v_q = R_s i_q + \frac{d\lambda_q}{dt} + \omega_e \lambda_d \quad (7)$$

$$\lambda_d = L_d i_d + \lambda_f \quad (8)$$

$$\lambda_q = L_q i_q \quad (9)$$

$$i_d = \frac{1}{L_d} \int (v_d - R_s i_d + \omega_e L_q i_q) dt \quad (10)$$

$$i_q = \frac{1}{L_q} \int (v_q - R_s i_q + \omega_e (L_d i_d + \lambda_f)) dt \quad (11)$$

where

$$\begin{aligned} R_s &= \text{stator resistance} \\ \omega_e &= \text{electrical rotational speed} \\ \lambda_d, \lambda_q &= d - q \text{ reference flux linkage} \\ \lambda_f &= \text{permanent magnet flux linkage} \\ L_d, L_q &= d - q \text{ reference inductance} \end{aligned}$$

The mechanical aspects of the PMSM were modeled using the electrically generated torque of the machine. The torque of a PMSM with varying inductance between the d and q axes is modeled using equation 12 [12]. The angular acceleration is found using Newton's Second Law, the electrically generated torque, the friction torque, and load torque. It is then used to find the rotation speed, ω_m , in equation 13. The friction coefficient used within this model was $B = 0.0025$ and was a rough estimate of the friction caused by bearings in the motor. Note that the mechanical and electrical rotational speeds vary depending on the number of pole pairs where $\omega_e = p\omega_m$.

$$T_e = \frac{3}{2}p(\lambda_f i_q + (L_d - L_q)i_d i_q) \quad (12)$$

$$\omega_m = \frac{1}{J} \int (T_e - T_L - B\omega_m) dt \quad (13)$$

where

T_e = electrically produced torque

T_L = load torque

p = number of pole pairs

B = coefficient of friction

J = moment of inertia

ω_m = mechanical rotational speed

Using these equations, the torque, speed, and stator currents are found from the voltage and electrical speed of the system allowing the PMSM to be modeled as shown in the Simulink model in Figure 8.

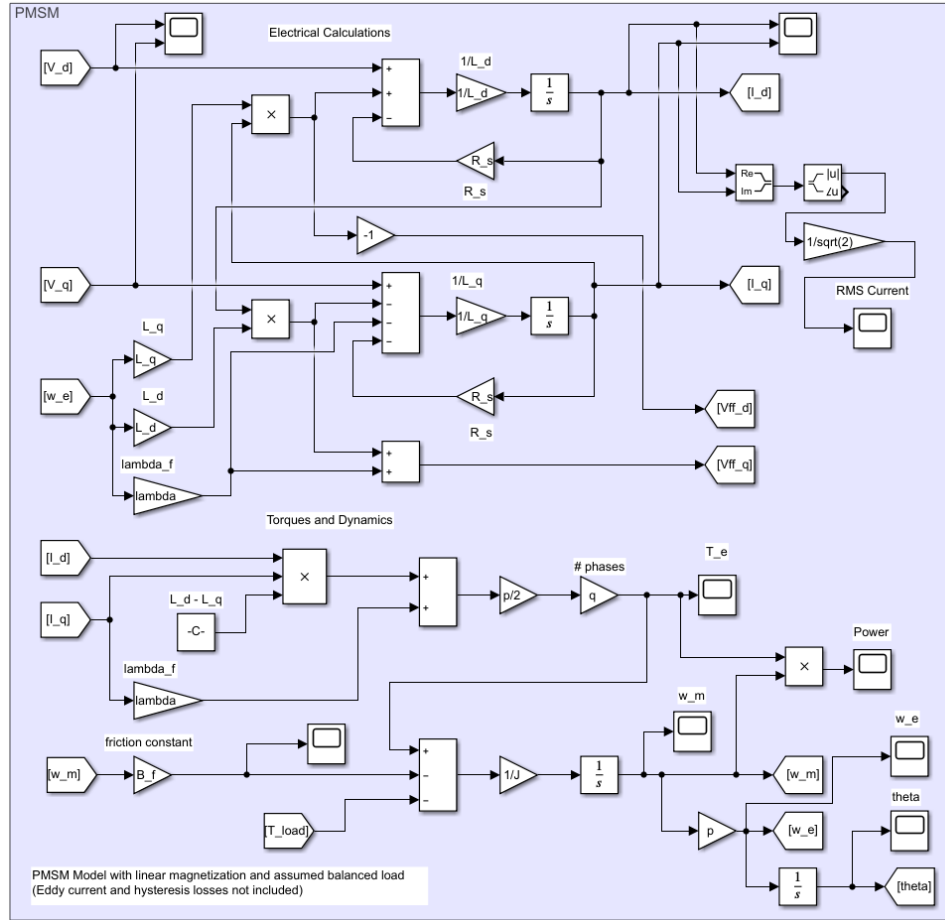


Figure 8 Permanent Magnet Synchronous Motor Simulink Model

As previously stated, the flight plan requires a rotational speed of 4929rpm while the rated speed of the motor is 4500rpm. A gear ratio of 0.75 was implemented into the system to decrease the required speed within the ratings of the motor. This ratio adjusts the speed and torque requirements on the motor to be 3697rpm and 318Nm. The gear ratio was chosen to keep the maximum planned speed within the rated speed while leaving some region of safety in the case of unexpected increases in speed from a sudden drop in load torque. A larger gear ratio would lead to a maximum

speed closer to the rated speed. This would reduce the required torque and current as well as improve the efficiency of the motor, but would also increase the required stator voltage towards the maximum provided by the battery. If this requirement exceeds the battery voltage, the motor will not be controlled properly and not meet the required torque and speed. The losses from the gearing implemented in this model were considered negligible.

B. Control and Inverter Modeling

The use of a PMSM requires a control method to adjust the speed and torque to fit the needs of the flight. A popular method used for many PMSMs is Field Oriented Control (FOC). FOC is a form of Vector Control that uses the same $d - q$ reference frame previously mentioned to control the torque output of the motor by adjusting the voltage and electrical frequency provided by the battery and inverter to the motor. Field Oriented Control fit this application well because of its quick response time and small torque ripple [13]; two features which were previously outlined as primary goals of the control method. The most efficient method of controlling the motor is a Maximum Torque Per Ampere (MTPA) control method. Magnetic torque is created by current in the q axis and is proportional to the permanent magnet flux linkage, λ_f , while reluctance torque is created by current in either axis and proportional to the difference in inductance between the d and q axes, $L_d - L_q$. Because of the small difference in inductance between the d and q axes and for simplicity, only magnetic torque was generated within this model. The MTPA method thus produced all its current in the q axis and none in the d axis.

FOC can also create a field weakening effect which weakens the field created by the magnets increasing the maximum speed that can be achieved while reducing the torque and power that can be produced at these speeds. Our flight always requires higher power along with a higher speed so the optimal operation of the motor is within the constant power region below the rated speed of the motor. Therefore field weakening is not used for our control method.

This FOC system was implemented using PI controllers for the comparison and regulation of the stator current and rotor speed. A block diagram showing the design of a FOC system with feed-forward voltage is shown in Figure 2.2 of [13]. The feed-forward voltage was included in the system as it improves the ability of the system to quickly respond to sudden changes in torque and current [14]. The first PI controller regulated the measured rotor speed with a desired rotor speed input to create a reference torque. The desired rotor speed was generated by the flight plan of the aircraft. This reference torque was then used to create a reference q axis current through the magnetic torque relation in equation 14. The zero-valued d reference current and calculated q reference current were used to compare and regulate the measured currents to create reference voltages. The total control system utilized three PI controllers for its regulation. The proportional and integral values for each controller were chosen arbitrarily to produce a seemingly reasonable response without wasting too much energy. Further work will be needed to optimize these control values. The d and q reference voltages were summed with the corresponding d and q feed-forward voltages which are calculated by equations 15 and 16 [13], then were limited by the maximum attainable phase voltage of the system. This system utilized a full bridge inverter. The maximum voltage was thus half of the average DC battery voltage. This output was then used to control the Space Vector Pulse Width Modulation (SVPWM). The full Simulink model of the Field Oriented Control is shown in Figure 9. Note that the feed-forward voltages were calculated within the PMSM model in Figure 8 and used within this controller model.

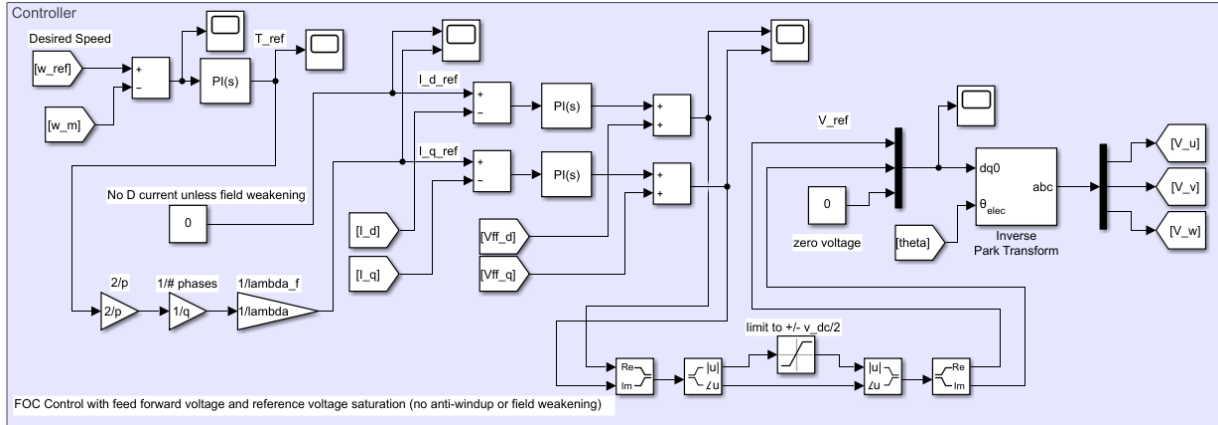
$$T_{mag} = \frac{3}{2} p \lambda_f i_q \quad (14)$$

$$v_{d,FF} = -\omega_e L_q i_q \quad (15)$$

$$v_{q,FF} = \omega_e (\lambda_f + L_d i_d) \quad (16)$$

SVPWM is a method of pulse width modulation that uses the desired three phase voltage values to create gate signals for an inverter. This method controls the inverter output voltage by changing the duty cycle of each leg of the inverter according to the value of that phase voltage. This system used the calculated FOC reference voltages and the Inverse Park Transform shown in equation 5 to create a three-phase desired voltage. These voltages were compared with the maximum phase voltage mentioned previously of half of the average battery DC voltage. This comparison was used to generate the duty cycle and gate signals for all six IGBTs (Insulated Gate Bipolar Transistors) used within the full bridge inverter. For more details about SVPWM, see [15].

The provided gate signals can create good approximations of sinusoidal signals at the output of the inverter making it useful for AC machines, but there are still some losses and high order effects from the switching. These effects were not included within this model and will be needed in the future to analyze efficiency and loss within the system. Instead,



C. Battery Modeling

The battery used within the powertrain makes up the majority of the total powertrain weight and thus was an important consideration in the design of the system. To minimize the total weight of the aircraft, a battery was chosen with a large specific energy. Lithium-ion batteries have some of the highest specific energies of currently available batteries and are the most used battery type for electric vehicles [16] making them well researched and safe. The chosen battery needed a high discharge rate as the takeoff and landing portions of the flight demand a large current. The chosen battery cell for this application was the Honcell Lithium-Ion Polymer HCG723496P Cell. The parameters for this cell are shown in Table 8 and [17]. Many of these parameters were not given explicitly by the supplier, but rather determined from provided discharge plots.

Nominal Voltage	3.58V
Average Voltage	3.7V
Full-Charge Voltage	4.15V
Exponential Voltage	3.7V
Nominal Capacity	2.4Ah
Maximum Capacity	2.85Ah
Exponential Capacity	1.5Ah
Rated Continuous Discharge	15C = 36A
Mass	67.0g
Size	34.4cm ³
Specific Energy	157.4Wh/kg
Energy Density	306.5Wh/l

Table 8 Grepow Lithium-Ion Polymer Battery Cell Parameters

To determine the number of cells necessary for this vehicle, an estimation of the required capacity was made. This estimate was made using the Simulink model with a constant battery voltage to determine the average current draw for each portion of the flight. This result, along with the time for each flight portion, was used to determine the total capacity needed from the battery. The motor requirements for each portion of the flight (with effects of the gear ratio included) along with the corresponding average current draw are shown in Table 9. The takeoff and landing requirements were generated using a standard helicopter propulsive power as specified within the motor modeling, the climb requirements were generated using a typical climb rate of commercial airliners of 5m/s, the cruise requirements were found using a drag buildup of an optimal individual found within the genetic algorithm with a method discussed in [18], and the glide requirements were found using an estimated power requirement of 90% of the cruise power. These general requirements were used along with the thrust (C_T) and power (C_P) coefficients mentioned earlier to find the torque and speed requirements of each motor for each phase of the flight.

Flight Phase	Flight Time (s)	Torque (Nm)	Rotor Speed (rpm)	Average Battery Current (A)
1 (Takeoff)	30	318	3697	191.9
2 (Climb)	44	57.3	1569	14.6
3 (Cruise)	2875	25.5	968	4.03
4 (Glide)	105	22.9	968	3.63
5 (Landing)	100	318	3697	191.9

Table 9 Motor Flight Requirements and Average Current

Using the average battery current, the time for each phase, and an additional safety factor of 1.25, the total required charge was estimated to be 13.04Ah. Knowing the average battery cell voltage of 3.7V, 176 cells were needed in series to reach the desired average 650V DC voltage. To reach the desired capacity of 13.04Ah, at least 6 cells were needed in parallel given each cell has a rated capacity of 2.4Ah. To reach the maximum current draw of the system of 191.6A, at least 6 cells were needed in parallel given each cell has a rated continuous discharge of 15C or 36A. This means 176

cells were required in series and 6 cells were required in parallel giving us a total of 1056 cells used for the battery of the powertrain for a single motor.

The lithium-ion battery has a dynamic voltage that changes with the current draw and with the total charge remaining within the battery. To model these cells, equation 20 represents the output voltage of the cell as a function of charge and current draw [12]. This equation assumes that the temperature of the battery and the internal resistance of the battery remain constant. The filtered current included in the last term of equation 20 can be expressed as shown in equation 21 and is affected by the diffusion resistance and capacitance within the battery as well as the dynamics of the battery current [19]. This model ignored the affects of dynamic battery current on battery voltage and instead only examined the steady-state battery current effects. Therefore, $i^* \approx i$. The affects of the current dynamics will be important for a higher level analysis of the powertrain, but were ignored for the preliminary sizing done within this model. For this model, it was also assumed that each battery cell behaves exactly the same. The voltage between each cell in series and current draw between each cell in parallel were the same allowing the model of a single cell to dictate the performance of the entire battery. The total DC current draw from the motor is determined by equation 22 [12]. This along with the battery voltage equation were used to model the battery as shown in Figure 11.

$$V_{bat} = E_0 - Ri - K \frac{Q}{Q - i_t} i_t + A e^{-B i_t} - K \frac{Q}{Q - i_t} i^* \quad (20)$$

$$i^* = i - 4R_d C_d \frac{di}{dt} \quad (21)$$

$$i_{dc} = \frac{3}{2} \left(\frac{v_d}{v_{dc}} i_d + \frac{v_q}{v_{dc}} i_q \right) \quad (22)$$

where

E_0 = battery constant voltage

K = polarization constant

Q = maximum battery capacity

$i_t = \int i dt$ = battery charge

R = internal resistance

i = DC battery current

i^* = filtered current

A = exponential zone amplitude

B = exponential zone time constant

R_d = diffusion resistance

C_d = diffusion capacitance

D. Simulation Results

The final simulation used the same flight requirements specified in Table 9 with a dynamic battery voltage. Instead of determining the average current for a short time frame as done in the previous simulation, this simulation was performed for the full duration of the flight plan and included a 5 second transition period between each flight phase. The speed error from the set requirements to the measured speed, the stator RMS current, the battery cell DC current, and battery cell charge usage for the duration of the flight are shown below in Figure 12. The averaged value within these plots is a moving average over 0.1 seconds to limit the effects of oscillations due to step size within the simulation. As can be seen, the rotor speed error returned to zero after each change in flight requirements meaning the desired speed and torque was reached for each portion of the flight. The RMS stator current stayed below the motor's rated continuous current of 190A for the majority of the flight. The stator current only exceeded this rating at takeoff and landing and each instance was less than the rated peak current of 400A and sustained for less than two minutes as specified by the motor data sheet. The averaged battery cell current, or the DC current divided amongst the parallel cells, remained below the rated continuous discharge current of 36A. The measured battery cell current exceeded this rating for short periods of time

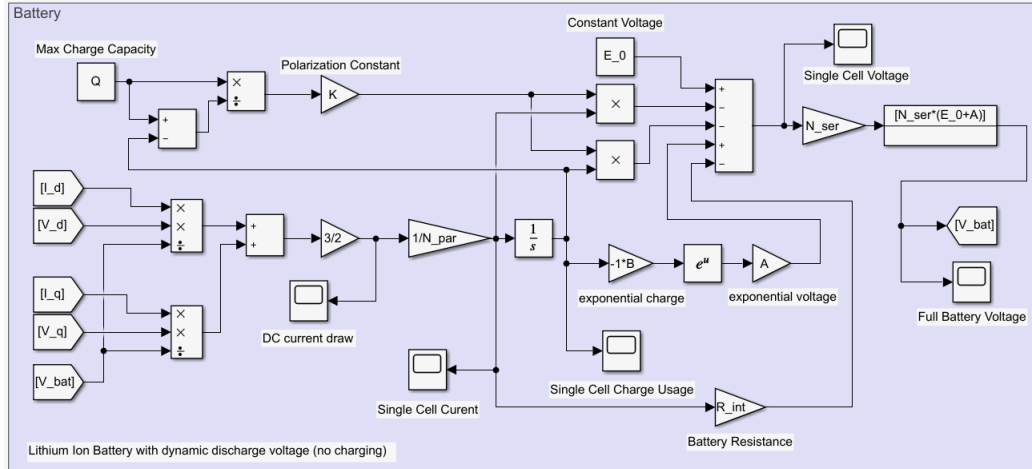


Figure 11 Lithium-Ion Battery Model

but always remained below the rated peak discharge rate of 30C or 72A. The system also did not use the total charge of each battery cell during the duration of the flight, staying below the nominal charge rating of 2.4Ah per cell. These considerations show that the flight was successful and safe within the ratings provided for each component of the system.

As each component within the system meets the flight requirements, sizing of the selected components within the powertrain was performed and compared to the previously estimated design. The model for the motor, inverter, battery, and control system all provided power and control for one of the 12 motors included on the aircraft. Therefore, the weight, size, and available power determined from this model were a twelfth of the total for the aircraft powertrain. The total size and weight of each component for the full powertrain is shown in Table 10 along with the initial weight estimates from [1]. Note that the power requirements of the system were increased from the proposed power requirements in [1]. The larger power requirements led to a larger motor weight than the initial estimate, but the high discharge rate of the selected battery led to a smaller battery weight than the initial estimate. Additionally, the total available peak power provided by the motors was about 2.25 MW. This maximum power was significantly higher than the aircraft's maximum power requirement of 1.47 MW and thus the sizing of the motor was larger than needed. The components used within this model are all currently available. Future technology will lead to the same performance with smaller and lighter components.

Component	Weight Estimate [1] (kg)	Weight (kg)	Size (l)
Motor	95.4	240	61.6
Battery	1217.7	849.0	436.2

Table 10 Selected Component Weight and Size

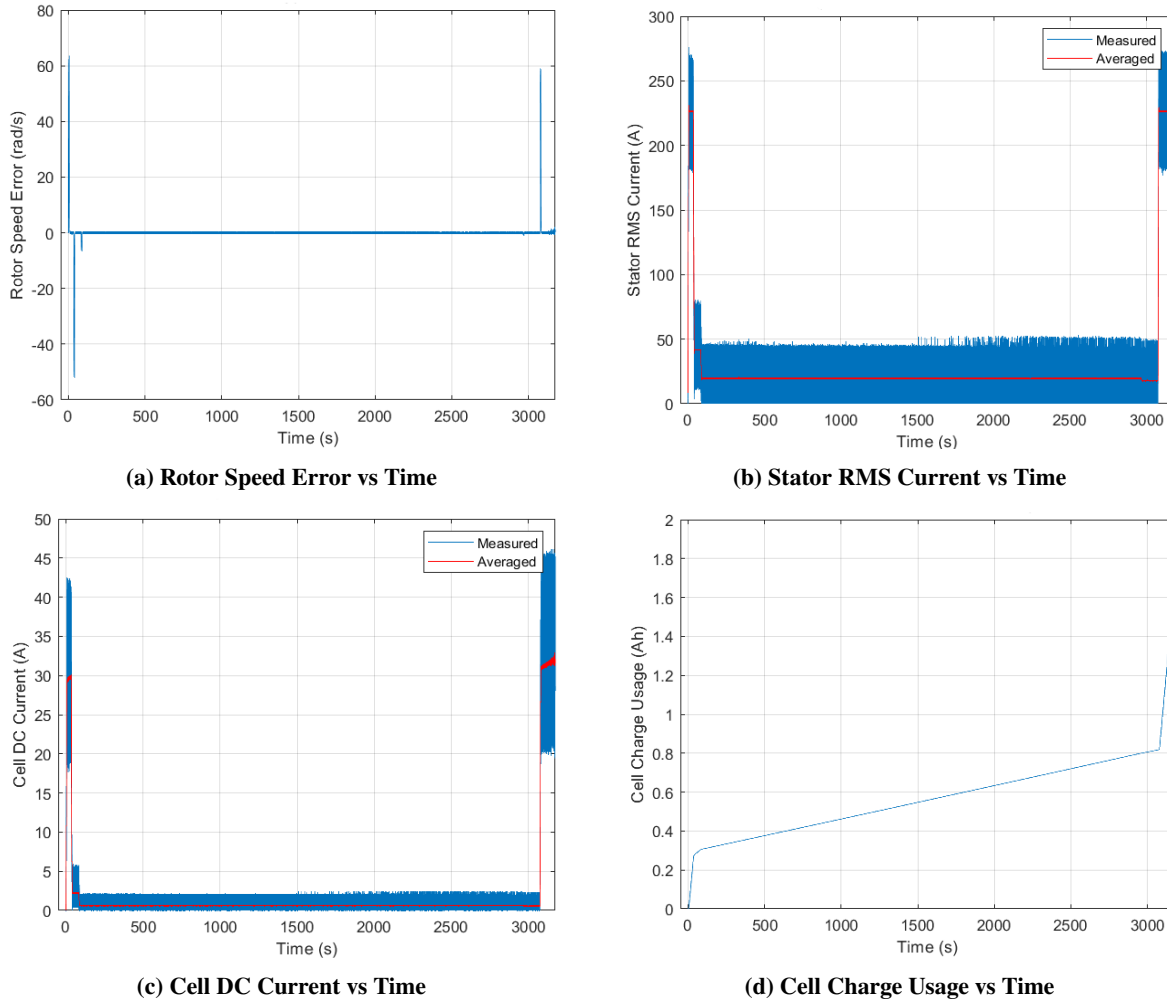


Figure 12 Powertrain Simulation Results

V. Conclusion

The purpose of this work was to design and analyze an optimal propulsion configuration for an eVTOL Air Shuttle. The results from this study point towards a vehicle capable of horizontal, stable flight at altitude.

The genetic algorithm generated a configuration that produced minimal drag by adjusting the wing positioning and wing size. Based on the results, while it is possible that certain combinations of positioning and sizing of the wings correlate to the decreasing total drag, it is not possible to independently attribute any correlation to any particular parameter.

The powertrain simulation showed a successful flight under the requirements generated using an optimal propulsion configuration. The simulation showed that all ratings of chosen components were met indicating the components were properly sized for the application. The weight estimate using these components shows a larger motor weight than originally anticipated, but a smaller battery weight leading to a similar total weight as estimated in [1].

The study justifies the feasibility of the tandem-wing design although future work could involve research into an optimal wing shape and the aerodynamic stability of the aircraft. This could include further exploration into the shape of the wings and other lifting and control surfaces of the aircraft as well as a center of gravity evaluation. Further modeling of the aircraft's aerodynamic performance in sub-optimal conditions as well as determining mechanisms for in-flight control should also be explored. As the design of the aircraft matures there will be greater insight into the exact aerodynamic characteristics, namely that of lift and drag, that will allow the work in this paper and all future research to be conducted with a higher degree of accuracy. Further improvements can be made to the powertrain model for better simulation of the performance as well as efficiency and loss calculations of the system. Within the motor,

these improvements include non-linear magnetization or saturation, hysteresis and eddy current losses, and higher order effects. Switching effects and losses can be included within the inverter with a detailed model. Optimized control parameters can be used to maximize the control efficiency and responsiveness. Additional control improvements can be made as well such as anti-windup or generation of reluctance torque using d-axis current. Improved battery can be achieved with the addition of dynamic current effects and current filtering. An optimized gearing ratio could also be included in the system to improve the efficiency of the motors. The model could include the thermal effects within the motor, inverter, and battery as the temperature affects the performance of all components. Lastly, transmission line and gearing losses could be modeled to further determine the losses within the system in full. Future technology will further improve the results of the powertrain sizing leading to the same available power with less weight. Potential sources of these improvements include Lithium-Metal battery technology as well as custom motor designs to better fit the needs of the aircraft.

References

- [1] Xiao, J., Salk, N., and Haran, K., "Conceptual Design of an eVTOL Air Shuttle for Rapid Intercity Transport," *2020 IEEE Power and Energy Conference at Illinois (PECI)*, 2020, pp. 1–8. <https://doi.org/10.1109/PECI48348.2020.9064631>.
- [2] Johnson, W., Silva, C., and Solis, E., "Concept Vehicles for VTOL Air Taxi Operations," *AHS Technical Conference on Aeromechanics Design for Transformative Vertical Flight*, 2018.
- [3] Harris, F., "Hover Performance of Isolated Propellers and Propellers - Experimental Data," 2017.
- [4] Kang, H., Genco, N., and Altman, A., "Analysis of fan stage conceptual design attributes for boundary layer ingestion," *Journal of Aircraft*, Vol. 50, No. 1, 2013.
- [5] Yang, Y., Zhou, T., Sciacchitano, A., Veldhuis, L., and Eitelberg, G., "Propeller and inflow vortex interaction: vortex response and impact on the propeller performance," *CEAS Aeronautical Journal*, Vol. 7, 2016.
- [6] Jones, R., and Cleaver, D., "Aerodynamics of Biplane and Tandem Wings at Low Reynolds Numbers," *Experiments in Fluids*, Vol. 56, No. 6, 2015.
- [7] Brinkworth, B., "On the aerodynamics of the Miles Libellula tandem-wing aircraft concept, 1941 – 1947," *Journal of Aeronautical History*, Vol. 02, 2016.
- [8] van der Geest, M., Polinder, H., Ferreira, J. A., and Christmann, M., "Power Density Limits and Design Trends of High-Speed Permanent Magnet Synchronous Machines," *IEEE Transactions on Transportation Electrification*, Vol. 1, No. 3, 2015. <https://doi.org/10.1109/TTE.2015.2475751>.
- [9] Lamperth, M. U., Malloy, A. C., Mlot, A., and Cordner, M., "Assessment of Axial Flux Motor Technology for Hybrid Powertrain Integration," *World Electric Vehicle Journal*, Vol. 7, 2015.
- [10] *Manual for EMRAX Motors / Generators: EMRAX 268 Technical Data Table*, EMRAX, March 2020. URL https://emrax.com/wp-content/uploads/2020/03/emrax_268_technical_data_table_graphs_5.4.pdf.
- [11] Massey, S., "Modeling, Simulation and Control of Hybrid Electric Vehicle Drive While Minimizing Energy Input Requirements Using Optimized Gear Ratios," *Michigan Technological University*, 2016. <https://doi.org/10.37099/mtu.dc.etr/133>.
- [12] Shukla, A., "Modelling and Simulation of Hybrid Electric Vehicles," *Imperial College London; Department of Mechanical Engineering*, 2012. <https://doi.org/10.25560/9761>.
- [13] Munoz, D. V., "Design, Simulation and Implementation of a PMSM Drive System," *Chalmers University of Technology; Department of Energy and Environment*, 2011.
- [14] Han, J., Gu, X., Yang, Y., and Tang, T., "Dynamic Improvement with a Feedforward Control Strategy of Bidirectional DC-DC Converter for Battery Charging and Discharging," *Electronics*, Vol. 9, No. 1738, 2020. <https://doi.org/10.3390/electronics9101738>.
- [15] Peddapelli, S. K., *Pulse Width Modulation: Analysis and Performance in Multilevel Inverters*, De Gruyter Oldenbourg, 2016. <https://doi.org/10.1515/9783110470420>.
- [16] Miao, Y., Hynan, P., von Jouanne, A., and Yokochi, A., "Current Li-Ion Battery Technologies in Electric Vehicles and Opportunities for Advancements," *Energies*, Vol. 12, No. 1074, 2019. <https://doi.org/10.3390/en12061074>.

- [17] *Rechargeable Lithium Ion Polymer Battery; Model Number: HCG-7834125P*, Shenzhen Honcell Energy Co., 2018. URL <http://www.honcell.com/Uploads/Temp/download/20180913/5b9a098bcdfeb.pdf>.
- [18] Sadraey, M., *Aircraft Performance: An Engineering Approach*, 1st ed., CRCPress, 2017.
- [19] Potrykus, S., Kutt, F., Nieznanski, J., and Jesus Fernandez Morales, F., “Advanced Lithium-Ion Battery Model for Power System Performance Analysis,” *Energies*, Vol. 13, No. 2411, 2020. <https://doi.org/10.3390/en13102411>.